

Roles of SN and AGN Feedback in Shaping the Baryonic Content in a Wide Range of Dark Matter Halo Mass

EMANUELE CONTINI,¹ CHANJO SEO,¹ JINSU RHEE,^{1,2,3} SEYOUNG JEON,¹ AND SUKYOUNG K. YI¹

¹*Department of Astronomy and Yonsei University Observatory, Yonsei University, 50 Yonsei-ro, Seodaemun-gu, Seoul 03722, Republic of Korea*

²*Institut d'Astrophysique de Paris, Sorbonne Université, CNRS, UMR 7095, 98 bis bd Arago, 75014 Paris, France*

³*Korea Astronomy and Space Science Institute, 776, Daedeokdae-ro, Yuseong-gu, Daejeon 34055, Republic of Korea*

ABSTRACT

We build upon **FEGA25** (Contini et al. 2025), a previously introduced semi-analytic model (SAM) for galaxy formation and evolution, by focusing on its enhanced treatment of supernova (SN) and active galactic nucleus (AGN) feedback mechanisms. In addition to the traditional AGN feedback mode—negative (suppressing cooling) and the new positive mode (triggering star formation)—we introduce two distinct implementations of a third mode: the ejection of hot gas beyond the virial radius (**AGNeject1** and **AGNeject2**). This component addresses a longstanding issue in SAMs and hydrodynamical simulations: the overestimation of hot gas fractions in low- and intermediate-mass halos. **FEGA25** is calibrated via MCMC using a suite of cosmological N-body simulations (YS50HR, YS200, YS300) and a comprehensive set of observed stellar mass functions across a wide redshift range. We find that SN feedback dominates gas ejection in halos with $\log M_{\text{halo}} \lesssim 12$, while AGN feedback becomes increasingly important at higher halo masses. The **AGNeject2** model, which activates primarily at late times ($z < 1$), reproduces a characteristic “cavity” (sort of U-shape) in the baryon fraction at $z = 0$, similar to trends observed in simulations like SIMBA and IllustrisTNG. Conversely, **AGNeject1** yields a smoother, redshift-independent evolution. Both models preserve the stellar and cold gas components and successfully reproduce the stellar-to-halo mass relation up to $z = 3$. Our results emphasize that a physically motivated AGN-driven mechanism capable of selectively removing hot gas is essential to model the baryon cycle accurately, particularly in the intermediate halo mass regime.

Keywords: galaxies: clusters: general (584) galaxies: formation (595) — galaxies: evolution (594) — methods: numerical (1965)

1. INTRODUCTION

In the current Λ CDM framework, galaxies form within dark matter (DM) halos that assemble hierarchically through mergers and smooth accretion (White & Rees 1978; Springel et al. 2005). While the growth of DM structures is well described by gravitational dynamics, the observable properties of galaxies depend critically on baryonic processes—namely gas cooling, star formation, chemical enrichment, and feedback. Among these, feedback from supernovae (SN) and active galactic nuclei (AGN) is widely regarded as essential for regulating

star formation, quenching massive galaxies, and explaining the observed galaxy stellar mass function (Guo et al. 2013; Somerville & Davé 2015; Naab & Ostriker 2017; Contini et al. 2019, 2020; Vogelsberger et al. 2020; Henriques et al. 2020).

Yet, despite the inclusion of increasingly sophisticated feedback prescriptions, models still struggle to simultaneously match key observables such as the cosmic star formation rate density (Madau & Dickinson 2014), the stellar-to-halo mass relation (Moster et al. 2013; Behroozi et al. 2019), and the distribution of hot and cold baryons across halo mass and redshift (Chiu et al. 2016; Eckert et al. 2021; Popesso et al. 2024). This tension is particularly severe in the group mass regime ($\log M_{\text{halo}} \sim 12.5\text{--}13.5$), where feedback must be pow-

erful enough to eject baryons, yet gentle enough not to alter the stellar and cold gas components.

Large-scale hydrodynamic simulations such as IllustrisTNG (Pillepich et al. 2018; Nelson et al. 2019), SIMBA (Davé et al. 2019), EAGLE (Schaye et al. 2015), MAGNETICUM (Dolag et al. 2016), and more recently FLAMINGO (Schaye et al. 2023) and MillenniumTNG (Pakmor et al. 2023), have offered valuable insights into feedback-regulated galaxy evolution. However, they often yield divergent predictions for baryon fractions and hot gas content, reflecting the sensitivity of such quantities to the underlying physics. For instance, while IllustrisTNG and SIMBA predict a baryon “cavity”—a depression in the baryon fraction at intermediate halo masses—other simulations such as MAGNETICUM show a smoother, power-law trend more consistent with X-ray and SZ observations (Hadzhiyska et al. 2024; Popesso et al. 2024).

Recent comparative analysis (Ayromlou et al. 2023; Salcido et al. 2023; Dev et al. 2024) have further demonstrated that baryon retention is highly dependent on the efficiency and coupling of feedback modes. These studies reinforce the need for physically motivated models that can selectively eject hot gas—especially in group-scale halos—without modifying the stellar and cold gas reservoirs (Eckert et al. 2021; Dev et al. 2024; Popesso et al. 2024).

In this context, semi-analytic models (SAMs) remain an indispensable tool. Their modular structure and computational efficiency allow for rapid exploration of parameter space and clearer isolation of physical mechanisms. Modern SAMs such as those developed by Lagos et al. (2024) and Contini et al. (2025) have adopted increasingly sophisticated AGN feedback prescriptions, including both radio-mode heating and direct ejection of hot gas. Notably, the SHARK2 model (Lagos et al. 2024) includes a formulation similar in spirit to one of our schemes.

Building on this foundation, we have developed the FEGA series (Contini et al. 2024, 2025), a SAM calibrated against a wide range of observational constraints. In particular, FEGA25 (Contini et al. 2025) introduced two key advancements: a physically motivated positive AGN feedback mode (triggering star formation under residual cooling), and a novel mechanism for ejecting hot gas beyond the virial radius. The latter is motivated by the need to reconcile models with observed hot gas fractions in low- and intermediate-mass halos, where supernova feedback alone appears insufficient (Henriques et al. 2013; Hirschmann et al. 2016; Ayromlou et al. 2023).

In this work, we investigate the impact of two distinct implementations of this hot gas ejection mode—AGNeject1, which scales with black hole accretion and halo virial velocity, and AGNeject2, which uses the surplus AGN energy beyond that needed to suppress cooling to drive ejection. We calibrate both models using cosmological DM-only simulations and an extensive set of observed stellar mass functions from $z = 3$ to the present (Marchesini et al. 2009, 2010; Ilbert et al. 2013; Muzzin et al. 2013; Tomczak et al. 2014; Bernardi et al. 2018).

We focus on three main goals: (i) to quantify the relative contributions of SN and AGN feedback in ejecting baryons beyond the virial radius; (ii) to assess the evolution of baryon and hot gas fractions as a function of halo mass and redshift; and (iii) to compare our predictions with hydrodynamic simulations and observational estimates, particularly those from recent X-ray and SZ studies (Chiu et al. 2016; Eckert et al. 2021; Angelinelli et al. 2023; Popesso et al. 2024).

Our analysis offers new insights into the physical mechanisms driving baryon depletion in halos and provides a framework for interpreting upcoming observational constraints. In particular, we argue that the inclusion of a physically motivated AGN-driven hot gas ejection channel is essential for reproducing both the amplitude and shape of baryon and hot gas fraction trends across halo mass—especially in the transition regime between SN- and AGN-dominated feedback.

In Section 2, we present the key features of FEGA25, highlighting the implementation of its AGN feedback modes and, in particular, the two alternative schemes for hot gas ejection—AGNeject1 and AGNeject2. We describe the set of cosmological N-body simulations used to generate DM halo merger trees, the observational constraints employed for calibration, and the methodology adopted for parameter tuning via Markov Chain Monte Carlo (MCMC). Moreover, part of the analysis will be complemented by results from our in-house NewCluster simulation, which will be briefly described.

In Section 3, we analyze the resulting galaxy catalogs and compare the predicted baryonic content—total baryon fraction, hot gas fraction, and stellar mass—with a comprehensive set of observations and hydrodynamic simulations. We quantify the efficiency of SN and AGN feedback in removing gas beyond the virial radius, assess the emergence of baryon depletion features such as the cavity, and evaluate the redshift evolution of these effects.

Finally, in Section 4, we summarize our main findings and discuss their implications for

galaxy formation theory and future observational efforts. Stellar masses are computed by adopting a [Chabrier \(2003\)](#) initial mass function, and unless otherwise specified, all masses are h-corrected.

2. METHODS

To achieve our goals, we employ the state-of-the-art semi-analytic model **FEGA25** (Formation and Evolution of GALaxies [Contini et al. 2025](#), hereafter C25), applied to a suite of three DM-only cosmological simulations. Additionally, we gain further insight from our high-resolution zoom-in simulation **NewCluster** ([Han et al. 2025b](#)). Below, we briefly outline the key features of our SAM, including the main physical prescriptions relevant to this study and, most notably, the new implementation of an alternative AGN-driven hot gas ejection mode, which represents a key innovation of this work. We also summarize the main characteristics of the **NewCluster** simulation. It is important to emphasize that in the analysis presented in Section [3Results and Discussion-section.3](#), we make limited use of **NewCluster** predictions, as a dedicated and more comprehensive study based on this simulation is currently in preparation (Seo et al.).

2.1. FEGA25

FEGA25 is an updated version of the SAM originally introduced in [Contini et al. 2024](#) (hereafter C24), featuring two major advancements: (i) a more sophisticated treatment of star formation that follows the Extended Kennicutt–Schmidt relation ([Shi et al. 2011](#)), and (ii) a novel implementation of positive AGN feedback, a mode that enhances star formation rather than suppressing it.

The main new feature introduced in **FEGA25** is a third mode of AGN feedback, specifically designed to eject hot gas beyond the virial radius of halos. This mechanism, referred to as the hot gas ejection mode, adds to the existing suite of feedback processes already present in the SAM. In this framework, gas can be expelled from halos via two channels: SN feedback and AGN-driven ejection.

The three AGN feedback (radio) modes, along with SN feedback, are the key physical processes governing baryon cycling in our model and are central to the present study. Below, we describe each of them in detail.

Finally, as mentioned above, we introduce an alternative implementation of the hot gas ejection mode. For clarity, we refer to the original version as **AGNeject1**, and to the updated one as **AGNeject2**.

2.1.1. SN feedback

SN feedback, resulting from the explosive deaths of massive stars, is a fundamental process in galaxy for-

mation and is central to the present model. This mechanism is particularly effective in regulating star formation in low-mass galaxies, shaping the low-mass end of the stellar mass function (SMF) and luminosity function (e.g., [Guo et al. 2010](#); [Henriques et al. 2013](#)) by limiting stellar mass growth in dwarfs. The energy released—both radiative and kinetic—can substantially impact the interstellar medium, leading to its heating and ionization. In some cases, this energetic input is sufficient to drive gas completely out of the galactic halo, making SN feedback a critical component in virtually all SAMs of galaxy formation. Historically, SN feedback has been maximized in such models because it has been essential to reproducing the observed evolution of the SMF’s low-mass slope (e.g., [Guo et al. 2011, 2013](#); [Henriques et al. 2013, 2015](#); [Hirschmann et al. 2016](#); [Contini et al. 2017](#); [Henriques et al. 2020](#)).

In **FEGA25**, SN feedback is implemented such that cold gas in the galactic disk is heated and transferred to the hot gas phase, and part of the hot gas is further expelled into an external reservoir. This approach follows the formulation of [Guo et al. \(2011\)](#), though we adopt different parameters, following [Hirschmann et al. \(2016\)](#), in which the feedback weakens over cosmic time.

In this framework, the amount of cold gas reheated by SN explosions and moved to the hot phase is given by:

$$\delta M_{\text{reh}} = \epsilon_{\text{reh}} \cdot \left[0.5 + (1+z)^3 \left(\frac{V_{\text{max}}}{V_{\text{reh}}} \right)^{-\beta_{\text{reh}}} \right] \cdot \delta M_*, \quad (1)$$

where $\epsilon_{\text{reh}} = 0.7$, $V_{\text{reh}} = 70 \text{ km/s}$, $\beta_{\text{reh}} = 3.5$, and δM_* represents the mass of newly formed stars. The inclusion of the variable ϵ_{reh} by [Guo et al. \(2011\)](#) allows for enhanced ejection efficiencies in dwarf galaxies. The total energy injected into the disk and halo gas is:

$$\delta E_{\text{SN}} = \eta_{\text{ej}} \cdot \left[0.5 + (1+z)^3 \left(\frac{V_{\text{max}}}{V_{\text{ej}}} \right)^{-\beta_{\text{ej}}} \right] \cdot \delta M_* \cdot 0.5 V_{\text{SN}}^2, \quad (2)$$

where $\eta_{\text{ej}} = 0.15$, $V_{\text{ej}} = 70 \text{ km/s}$, $\beta_{\text{ej}} = 3.5$, and $0.5 V_{\text{SN}}^2$ represents the average kinetic energy of SN ejecta per unit mass of stars formed, calculated based on $V_{\text{SN}} = 630 \text{ km/s}$ ([Croton et al. 2006](#)). From this energy amount, the ejected gas (including metals) from the halo is:

$$\delta M_{\text{ej}} = \frac{\delta E_{\text{SN}} - 0.5 \delta M_{\text{reh}} V_{200}^2}{0.5 V_{200}^2}. \quad (3)$$

The ejected material populates the ejecta reservoir and may be reincorporated at later stages (see C24 for further details).

2.1.2. Negative and Positive AGN feedback

The radio mode of AGN feedback in our model follows the original prescription of [Croton et al. \(2006\)](#). In this mode, hot gas accretes onto the central black hole (BH), releasing mechanical energy that heats the surrounding halo gas. The accretion rate is given by:

$$\dot{M}_{\text{BH}} = \kappa_{\text{AGN}} \left(\frac{f_{\text{hot}}}{0.1} \right) \left(\frac{V_{200}}{200 \text{ km/s}} \right)^3 \left(\frac{M_{\text{BH}}}{10^8 M_{\odot}/h} \right) \quad (4)$$

where f_{hot} is the hot gas fraction (relative to halo mass), and κ_{AGN} is a free parameter tuned during calibration to regulate accretion efficiency.

The energy released through this process is:

$$\dot{E}_{\text{radio}} = \eta_{\text{rad}} \dot{M}_{\text{BH}} c^2, \quad (5)$$

with $\eta_{\text{rad}} = 0.1$ and c being the speed of light. This energy injection offsets gas cooling, leading to a revised cooling rate:

$$\dot{M}_{\text{cool,new}} = \dot{M}_{\text{cool}} - 2 \frac{\dot{E}_{\text{radio}}}{V_{200}^2}, \quad (6)$$

Depending on the AGN power, cooling may be partially or fully suppressed—concluding the negative AGN feedback phase. Traditionally, SAMs channel the net cooled mass into the cold gas reservoir for star formation. However, in **FEGA25**, this component undergoes an additional feedback process: the positive mode.

Introduced in C24, the positive AGN feedback simulates a secondary starburst triggered by AGN-driven pressure. This effect, while supported by both observational (e.g., [Cresci et al. 2015](#); [Mahoro et al. 2017](#); [Joseph et al. 2022](#)) and theoretical studies ([Gaibler et al. 2012](#); [Silk 2013](#); [Mukherjee et al. 2018](#)), was initially modeled in a simplified way to test its impact, but introducing new free parameters.

In **FEGA25**, we maintain this minimal approach. The positive feedback mode uses the same parameters as the negative mode and is only triggered if some residual cooling occurs ($\dot{M}_{\text{cool,new}} > 0$). The resulting star formation rate from this mode is given by:

$$\dot{M}_{*} = \left(\frac{\delta M_{\text{BH}}}{M_{\text{BH}}} \right) \left(\frac{\dot{M}_{\text{cool,new}}}{10^8 M_{\odot}/h} \right), \quad (7)$$

where δM_{BH} is the BH mass growth due to accretion (Eq. [4Negative and Positive AGN feedback equation.2.4](#)).

This new formulation (implemented in C25) improves on the earlier version (the original one in C24) by tying the efficiency of the positive mode directly to BH

accretion, which is itself regulated by κ_{AGN} . This ensures that both AGN feedback modes are consistently governed by a single parameter. It also introduces a natural coupling between them: the positive mode becomes prominent when the negative one is weak (e.g., at high redshift), and diminishes as the negative feedback grows stronger over time.

2.1.3. AGNeject1 and AGNeject2

In C25, we outlined a longstanding difficulty in SAMs (but also in hydrodynamic simulations): their failure to accurately reproduce the fraction of hot gas in halos, along with a proposed strategy to resolve it. This solution requires a mechanism capable of removing part of the hot gas beyond the virial radius, while leaving cooling and star formation processes unaffected. That is, the mechanism should extract hot gas without altering the cold gas or stellar components. To achieve this, we introduced a novel AGN feedback channel in **FEGA25**, referred to as the hot gas ejection mode, **AGNeject1**.

Inspired by the same rationale used in C24 to isolate the positive feedback effect, we postulate that such a mechanism is physically feasible and posit that the AGN can remove a portion of the hot gas, transferring it to an “ejected” reservoir. In our SAM, the amount of expelled hot gas is assumed to scale with the efficiency of the two other AGN feedback modes, through the parameter κ_{AGN} , and to be modulated by the virial velocity of the host halo. This ensures that expelling gas becomes increasingly difficult in more massive systems. The mass of hot gas expelled in **FEGA25** is computed via:

$$M_{\text{ejected}} = \left(\frac{\delta M_{\text{BH}}}{M_{\text{BH}}} \right) \left(\frac{M_{\text{hot}}}{10^8 M_{\odot}/h} \right) \left(1 - \frac{V_{200}}{V_{\text{scale}}} \right), \quad (8)$$

where V_{scale} is a tunable parameter determined during model calibration, and it sets the threshold at which this ejection becomes efficient¹. High values of V_{scale} make gas ejection more effective in massive halos, whereas low values diminish efficiency in low-mass halos. The computed ejected mass, M_{ejected} , is stored in an external reservoir but remains eligible for future reincorporation, consistent with the treatment described in C24. Naturally, when $V_{200} > V_{\text{scale}}$, the ejected mass is set to zero.

As discussed earlier, negative AGN feedback can, in certain regimes, deliver enough energy to entirely offset gas cooling, effectively reheating gas to the virial

¹ This prescription remains valid even when $\dot{M}_{\text{cool}} > 2 \frac{\dot{E}_{\text{radio}}}{V_{200}^2}$, i.e., when the AGN energy input is insufficient to fully suppress gas cooling.

temperature. However, in cases where the energy released by the AGN surpasses what is needed to quench the cooling flow, it is plausible that this surplus energy could drive gas out of the halo. We propose here, and this is **AGNeject2**, that the excess energy, beyond what is required to halt cooling, may be responsible for ejecting gas outside the virial boundary.

Analogously to the implementation in **AGNeject1**, we assume that gas ejection becomes progressively more challenging in more massive halos—specifically, it is governed by the virial velocity of the host halo. Consequently, in cases where $\dot{M}_{\text{cool}} < 2 \frac{\dot{E}_{\text{radio}}}{V_{200}^2}$, the surplus energy is assumed to expel a portion of the excess gas mass, M_{excess} , which would otherwise have been reheated to the virial temperature. The amount of ejected mass is computed using the following expression:

$$M_{\text{ejected}} = M_{\text{excess}} \left(1 - \frac{V_{200}}{V_{\text{scale}}} \right), \quad (9)$$

with V_{scale} that must be determined with a separate calibration.

In summary, the full AGN feedback framework implemented in **FEGA25** consists of three components: the negative mode, the positive mode, and the hot gas ejection mode, either **AGNeject1** or **AGNeject2**. Compared to the version presented in C24, **FEGA25** introduces a more physically motivated description of the positive feedback (see Equation 7Negative and Positive AGN feedback equation.2.7) and adds a new prescription for the ejection of hot gas (Equations 8AGNeject1 and AGNeject2 equation.2.8 or 9AGNeject1 and AGNeject2 equation.2.9). As a result, **FEGA25** stands out as the only SAM that incorporates both a treatment of AGN-driven positive feedback and a mechanism for the ejection of hot gas. It must be noted, however, that an implementation similar to **AGNeject2** is incorporated in SHARK2 SAM (Lagos et al. 2024).

Our objective is to investigate the differences between the two hot gas ejection modes and, more importantly, to assess the relative roles of SN and AGN feedback in expelling hot gas beyond the virial radius across a wide range of halo masses.

2.1.4. Set of Simulations and Calibration

Calibrating a SAM is a fundamental step, particularly given that the physical prescriptions governing galaxy formation typically involve numerous parameters that are either loosely constrained by observations or entirely unknown. We calibrate **FEGA25** following the same procedure adopted in C25—namely, employing a Markov Chain Monte Carlo (MCMC) method. For a comprehensive explanation of this method, including its strengths,

limitations, and a discussion of alternative strategies, we refer the reader to C24, Henriques et al. (2020), and references therein.

The calibration of **FEGA25** relies on the same compilation of observed SMFs used in C24 and C25, spanning redshifts from $z = 3$ down to $z = 0$. This dataset brings together measurements from several observational studies, offering a robust picture of the SMF over time. Specifically, we use data points at $z = 3$, $z = 2.75$, $z = 2$, $z = 1.75$, $z = 1$, $z = 0.75$, $z = 0.4$, and $z = 0$, with high-redshift SMFs taken from Marchesini et al. (2009), Marchesini et al. (2010), Ilbert et al. (2010), Sánchez et al. (2012), Muzzin et al. (2013), Ilbert et al. (2013), and Tomczak et al. (2014). The SMF at $z = 0$ is compiled from Baldry et al. (2008), Li & White (2009), Baldry et al. (2012), and Bernardi et al. (2018). To complete the calibration pipeline and generate galaxy catalogs, we make use of cosmological N-body simulations, which provide the merger trees—the structural backbone of the SAM—containing essential information about the evolution of DM halos where galaxies reside.

We utilize three simulations: the YS50HR box, with a comoving volume of $(50 \text{ Mpc}/h)^3$, is used during the initial calibration phase, a larger YS200 box, with a volume of $(200 \text{ Mpc}/h)^3$, is employed for the final calibration, and a new run YS300, with a volume of $(300 \text{ Mpc}/h)^3$. All simulations cover the redshift range from $z = 63$ to $z = 0$, with 100 snapshots distributed between $z = 20$ and the present. They are run using GADGET4 (Springel et al. 2021), adopting cosmological parameters from the Planck 2018 results (Planck Collaboration et al. 2020): $\Omega_m = 0.31$ (total matter density), $\Omega_\Lambda = 0.69$ (dark energy density), $n_s = 0.97$ (scalar spectral index), $\sigma_8 = 0.81$ (amplitude of matter fluctuations), and $h = 0.68$ (Hubble parameter normalized to $100 \text{ km s}^{-1} \text{ Mpc}^{-1}$). The corresponding mass resolutions are $M_{\text{DM,part}} = 10^7 M_\odot/h$, $3.26 \cdot 10^8 M_\odot/h$, and $2.2 \cdot 10^9 M_\odot/h$ for the YS50HR, YS200, and YS300 simulations, respectively. For additional details on the overall setup and construction of the simulations, we refer the reader to Contini et al. (2023).

In line with the approach adopted by C25, the parameters constrained during the calibration process are: the AGN efficiency parameter κ_{AGN} appearing in Equation 4Negative and Positive AGN feedback equation.2.4, the scale velocity V_{scale} in Equation 8AGNeject1 and AGNeject2 equation.2.8, and the reincorporation factor

γ_2 .² The calibration of the SAM using the **AGNject1** prescription has already been performed in C25; therefore, in this work, we focus solely on calibrating the model with the **AGNject2** option enabled. The calibrated parameter values obtained are as follows for **AGNject1** (**AGNject2**): $\kappa_{\text{AGN}} = 2 \times 10^{-5}$, $(5 \times 10^{-5}) M_{\odot}/\text{yr}$; $V_{\text{scale}} = 500, (415) \text{ km/s}$; and $\gamma_2 = 0.378, (0.367)$.

We run the models on the merger trees extracted from all three simulations to generate our final galaxy catalogs. Due to the varying resolutions of the simulations, we apply different mass thresholds when selecting halos: specifically, we consider halos with $\log M_{200} > 11.0$ in YS50HR, $\log M_{200} > 12.0$ in YS200, and $\log M_{200} > 14.0$ in YS300. The combination of these subcatalogs forms our final, comprehensive catalogs.

2.2. *NewCluster*

NewCluster simulation (Han et al. 2025b) is a high-resolution cosmological zoom-in run designed to study galaxy formation in a massive cluster environment. It uses the **RAMSES-yOMP** code (Han et al. 2025a), a hybrid-parallelized version of the **RAMSES** hydrodynamics solver (Teyssier 2002), and focuses on the evolution of a region centered on a galaxy cluster with a virial mass of approximately $5 \times 10^{14} M_{\odot}$ at redshift $z = 0$. The simulation starts from a periodic box of $100 \text{ Mpc}/h$ and zooms in on a region of radius $\sim 17.7 \text{ Mpc}/h$, corresponding to $3.5 R_{\text{vir}}$.

In the zoom-in region, the mass resolution is $m_{\text{DM}} = 1.6 \times 10^6 M_{\odot}$ for dark matter and $m_* = 2 \times 10^4 M_{\odot}$ for stellar particles. The spatial resolution ranges from 53 to 107 parsecs, depending on the expansion factor. The adopted cosmology follows WMAP-7 parameters: $H_0 = 70.3 \text{ km s}^{-1} \text{ Mpc}^{-1}$, $\Omega_m = 0.272$, $\Omega_{\Lambda} = 0.728$, $\sigma_8 = 0.810$, and $n_s = 0.967$ (Komatsu et al. 2011).

Radiative processes are modeled assuming collisional ionization equilibrium. Metal-line cooling allows gas to cool below 10^4 K , and additional dust cooling is implemented. A uniform UV background is turned on at $z = 10$, with self-shielding based on the gas density.

Star formation occurs in gas with number density $n_{\text{H}} > 5 \text{ cm}^{-3}$ using a thermo-turbulent efficiency model. The simulation tracks nine chemical elements (H, D, C, N, O, Mg, Fe, Si, S), with yields from Type II and Type Ia supernovae and stellar winds. It adopts the Chabrier

(2003) initial mass function. SN II yields are based on Kobayashi et al. (2006), while SN Ia yields come from Iwamoto et al. (1999). Each SN Ia injects 10^{51} erg of energy. Feedback from both SN types is implemented using the mechanical model by Kimm & Cen (2014), and stellar winds are included following Leitherer et al. (1999).

AGN feedback is modeled with a dual-mode approach (Dubois et al. 2012), where black holes inject kinetic energy (jet mode) when the Eddington ratio $f_{\text{Edd}} < 0.01$, and thermal energy (quasar mode) for $f_{\text{Edd}} > 0.01$. The Eddington ratio is capped at 1.

A complete description of the simulation is provided in Han et al. (2025b).

3. RESULTS AND DISCUSSION

In the following sections, we use our catalogs to carry out three main analysis: (1) to investigate the baryonic content of dark matter halos, (2) to quantify the relative contributions of SN and AGN feedback in ejecting hot gas beyond the virial radius, and (3) to compare our predictions with hydrodynamic simulations and observational estimates. Predictions from our models, including those from **NewCluster**, will be compared with results from other simulations as well as a wide range of observational data, followed by a detailed discussion of the implications. We emphasize that, unless otherwise stated, all model predictions are presented as median values, with the 16th and 84th percentiles shown when possible.

3.1. *The Baryonic Content in DM Halos*

We begin our analysis in Figure 1, **The Baryonic Content in DM Halos**, which shows the baryon fraction—normalized to the universal value (Y_{200})—as a function of halo mass for the **AGNject1** (left panel) and **AGNject2** (right panel) models. Solid lines represent model predictions at different redshifts, while filled circles correspond to results from our **NewCluster** simulation. We also include observational estimates from Chiu et al. (2016) at $z \sim 0.9$, and Akino et al. (2022) at $0 < z < 1$, along with predictions from the **MAGNETICUM** simulation (Dolag et al. 2016) by Angelinelli et al. (2023), with symbols as indicated in the legend.

A caveat should be noted: while our predictions are based on Y_{200} and M_{200} , both the observational and simulation data used for comparison refer to Y_{500} . Since the baryon content within R_{500} is necessarily smaller than within R_{200} , these external datasets should be interpreted as lower limits.

Focusing first on the comparison between our models, **AGNject1** shows little redshift evolution, with only

² This parameter governs the rate at which ejected gas returns to the hot gas phase within the virial radius, and is defined by the relation: $\dot{M}_{\text{ej}} = \gamma_2 \frac{M_{\text{ej}}}{t_{\text{reinc}}}$, where M_{ej} represents the amount of gas in the ejected reservoir, and t_{reinc} is the reincorporation timescale. Further details are available in C24.

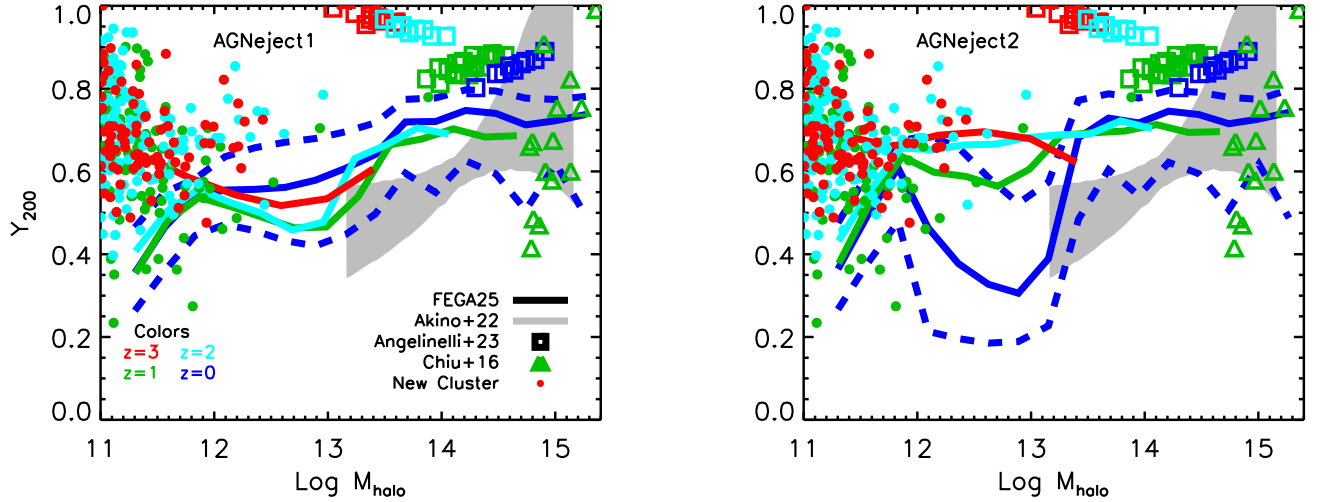


Figure 1. Baryon fraction, normalized to the universal value (Y_{200}), as a function of halo mass for the AGNeject1 (left panel) and AGNeject2 (right panel) models. Solid lines in different colors represent predictions at various redshifts, and are compared with results from our NewCluster simulation (filled circles), along with observational and simulation data from the literature (symbols as indicated in the legend). AGNeject1 shows little to no evolution across redshift, whereas AGNeject2 predicts a significant decline in baryon content with time in the range $11.8 < \log M_{\text{halo}} < 13.4$. At small scales, NewCluster supports the near-constant evolution suggested by AGNeject1. On cluster scales, both models agree reasonably well with the observations by Chiu et al. (2016) and Akino et al. (2022), but fall below the values reported by Angelinelli et al. (2023). The key difference between the models lies in the deep cavity at $z = 0$ (blue line) in AGNeject2, highlighting a stronger late-time depletion of baryons.

mild variation in a order of magnitude centered around $\log M_{\text{halo}} \sim 12.7$ – 12.8 . At lower halo masses, the predictions from NewCluster closely follow the nearly constant trend suggested by AGNeject1. At $z = 0$, the baryon fraction increases from about 0.4 at $\log M_{\text{halo}} \sim 11.2$ to roughly 0.75 for the most massive halos, reflecting a clear correlation with halo mass.

In contrast, AGNeject2 exhibits a more pronounced redshift dependence over the mass range $11.8 < \log M_{\text{halo}} < 13.4$, especially between $z = 1$ and the present. This results in a distinct “cavity” in the baryon fraction at $z = 0$ within that range. Outside this interval, the two models predict similar baryon fractions, indicating that the differences arise primarily at intermediate halo masses and late times—consistent with a more efficient, redshift-dependent removal of baryons in AGNeject2.

Compared to MAGNETICUM, both models predict lower baryon fractions—expected given the different apertures—but they are broadly consistent with observational data from Chiu et al. (2016) and Akino et al. (2022) for halos above $\log M_{\text{halo}} \sim 13$, even accounting for the likely upward correction needed in the observed values.

Baryons in our models are distributed among four main components: stars (including both those bound to galaxies and the intracluster light), cold and hot gas within the virial radius, and ejected gas—namely, hot

gas residing outside the virialized region. As shown in Figure 1, the total baryon fraction spans values between approximately 0.4 and 0.75, indicating that a substantial fraction of baryons is located beyond the virial boundary.

To investigate the gaseous component in more detail, Figure 2 displays the normalized hot gas fraction as a function of halo mass, with predictions from AGNeject1 (blue lines) and AGNeject2 (red lines) across different redshifts (each shown in separate panels). These are compared to predictions from the NewCluster simulation and a compilation of observational data from the literature: brown stars from Vikhlinin et al. (2006), Arnaud et al. (2007), Sun et al. (2009), Rasmussen & Ponman (2009), Pratt et al. (2009), Mahdavi et al. (2013), Gonzalez et al. (2013), Lovisari et al. (2015), Eckert et al. (2016), Pearson et al. (2017), Eckert et al. (2019), Mulroy et al. (2019), and Ragagnin et al. (2022); magenta diamonds from Popesso et al. (2024); green diamonds from Chiu et al. (2016); a grey shaded region from Eckert et al. (2021); a pink shaded region from Dev et al. (2024); and predictions from the MAGNETICUM simulation.

Before delving into the results, we note an important caveat. As in Figure 1, many of the observational estimates and MAGNETICUM predictions refer to gas fractions mea-

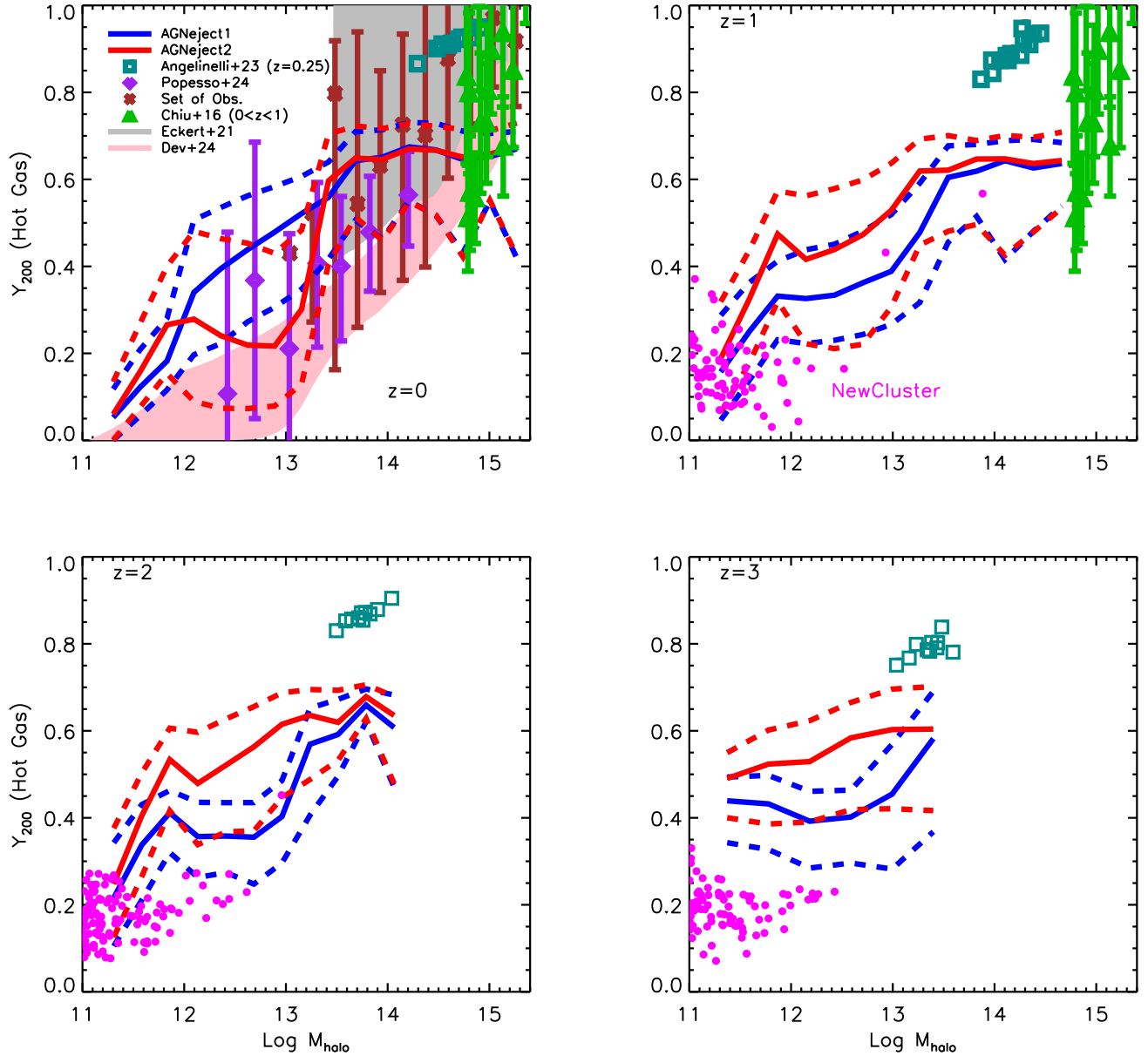


Figure 2. Hot gas fraction, normalized to the universal baryon fraction, as a function of halo mass at different redshifts (separate panels), as predicted by our models *AGNject1* (blue lines) and *AGNject2* (red lines). The predictions are compared to both observational constraints and simulation results at $z = 0$ and $z = 1$, and to simulations at higher redshifts. Results from our *NewCluster* simulation are also shown at $z \geq 1$ as filled magenta circles. Both models are broadly consistent with observations at $z = 0$ and show signs of convergence at $z = 1$, though they generally predict lower hot gas fractions than those found in the MAGNETICUM simulation (Angelinelli et al. 2023) across all redshifts. The main difference between the two models emerges in Milky Way–like halos (comparable to the mass range discussed in Figure 1The Baryonic Content in DM Halosfigure.1). *AGNject1* is more efficient at ejecting hot gas down to $z = 1$, while *AGNject2* becomes more efficient in the last ~ 7 Gyr. At $z = 3$, *NewCluster* predicts slightly lower hot gas fractions compared to the models, but overall follows the same qualitative trends. This evolution explains the deep cavity observed in the baryon fraction at $z = 0$ for *AGNject2*, as seen in Figure 1The Baryonic Content in DM Halosfigure.1.

sured within R_{500} , rather than R_{200} . Unlike the case of total baryons, however, a correction can be applied to translate Y_{500} values into their Y_{200} equivalents. To perform this conversion, we used the empirical relations provided by Popesso et al. (2024), which link Y_{200} to

R_{200} and Y_{500} to R_{500} , based on fits to their data. This allows us to compare our model predictions directly to the corrected observational estimates shown in Figure 2The Baryonic Content in DM Halosfigure.2.

Focusing first on $z = 0$, where observational constraints are most abundant, we find that the difference between the two AGN feedback models—previously identified as a cavity in Figure 1 *The Baryonic Content in DM Halos* figure.1—is entirely attributable to a more pronounced ejection of hot gas in AGNeject2 relative to AGNeject1. Outside of the intermediate mass range affected by this process, both models predict nearly identical hot gas fractions, consistent with their similar total baryon fractions. Importantly, despite the intrinsic scatter in the data, both models agree well with observations over a wide halo mass range, from $\log M_{\text{halo}} \sim 12.5$ up to the most massive clusters. Once again, the MAGNETICUM simulation tends to overpredict the hot gas content relative to our models.

At higher redshift, in particular at $z = 1$, we start to see the difference between our models: AGNeject1 predicts a lower hot gas fraction than AGNeject2 in the mass range corresponding to the cavity at the present time. This is because AGNeject1 is effective from early times down to $z = 0$, whereas AGNeject2 becomes highly effective only after $z \sim 1$. However, given the constancy of the hot gas fraction on cluster scales, our predictions remain consistent with the observations by Chiu et al. (2016), although they do not match those from MAGNETICUM, which show a constant trend even at higher redshift (see bottom panels). NewCluster, on the other hand, aligns well with our models at small scales up to $z = 2$, but this agreement breaks down at $z = 3$.

Comparing our results qualitatively with earlier studies—specifically C25 and Popesso et al. (2024)—we find similar conclusions. These authors emphasized the necessity, in numerical models, of a feedback mechanism capable of ejecting hot gas from halos without significantly altering the stellar and cold gas components. This is precisely what our models achieve, as the next plot will illustrate. Nonetheless, it remains challenging to distinguish between the two models due to the scarcity of observational data at $z > 1$ in the halo mass range where the cavity begins to develop—a feature entirely driven by more efficient hot gas expulsion.

One final point worth noting is that the normalized hot gas fraction at $z = 0$ —where observational coverage is most comprehensive—rises from roughly 0.3 at $\log M_{\text{halo}} \sim 12$ to about 0.65 in the most massive clusters. Comparing these figures with the total baryon fractions (which include cold gas and stars), we infer that, on cluster scales, approximately 92%-93% of the baryons reside in the hot phase, with this percentage declining toward lower halo masses. As previously shown in C25,

on smaller scales, both the stellar and cold gas components become more significant.

We conclude this section by demonstrating that our models also accurately predict the stellar content of halos. This is shown in Figure 3 *The Baryonic Content in DM Halos* figure.3, which displays the stellar-to-halo mass relation for central galaxies at various redshifts (panels), with our models color-coded as in the previous figure. At $z = 0$, we compare our results to the SHARK2 SAM (Lagos et al. 2024, black dashed lines), the empirical relation by Moster et al. 2013 (gray shaded region), and observational data from Romeo et al. 2020 (brown diamonds), Hinshaw et al. 2013, Gonzalez et al. 2013, and Kravtsov et al. 2018 (magenta squares). Both of our models match these datasets and the empirical relation very well, with no visible difference between them across the entire halo mass range.

At higher redshift, we compare our models with predictions from NewCluster (magenta filled circles) and the Moster et al. (2013) relation. Our models follow the empirical relation remarkably well up to $z = 3$, underscoring their ability to predict the correct stellar mass of central galaxies across all halo masses and cosmic times. NewCluster, by contrast, appears to overpredict stellar masses at all redshifts by approximately an order of magnitude. The origin of this discrepancy will be investigated in detail in Seo et al., in prep.

Focusing solely on the predictions from our SAM, both models successfully reproduce the stellar-to-halo mass relation at every redshift considered. This is important because stars are one of the three components used in computing the baryon fraction, meaning that our models accurately describe at least this component. Furthermore, given that the tension between model predictions and observations in both the baryon and hot gas fractions arises primarily at small group scales—and considering that stellar mass is a good tracer of the total stellar content at those scales, where cold gas is negligible—we conclude that the discrepancies are driven entirely by how much hot gas is expelled by feedback processes.

Again, this conclusion is in line with the arguments made in C25 and Popesso et al. (2024), which can be summarized succinctly: the physical mechanism(s) responsible for ejecting hot gas outside halos must not disturb the stellar or cold gas components. Our two models achieve this in different ways and with varying strengths over time. With this established, we now move on to investigate the two feedback mechanisms capable of ejecting hot gas—SN and AGN feedback—to determine which dominates, when, and in which halo mass regime.

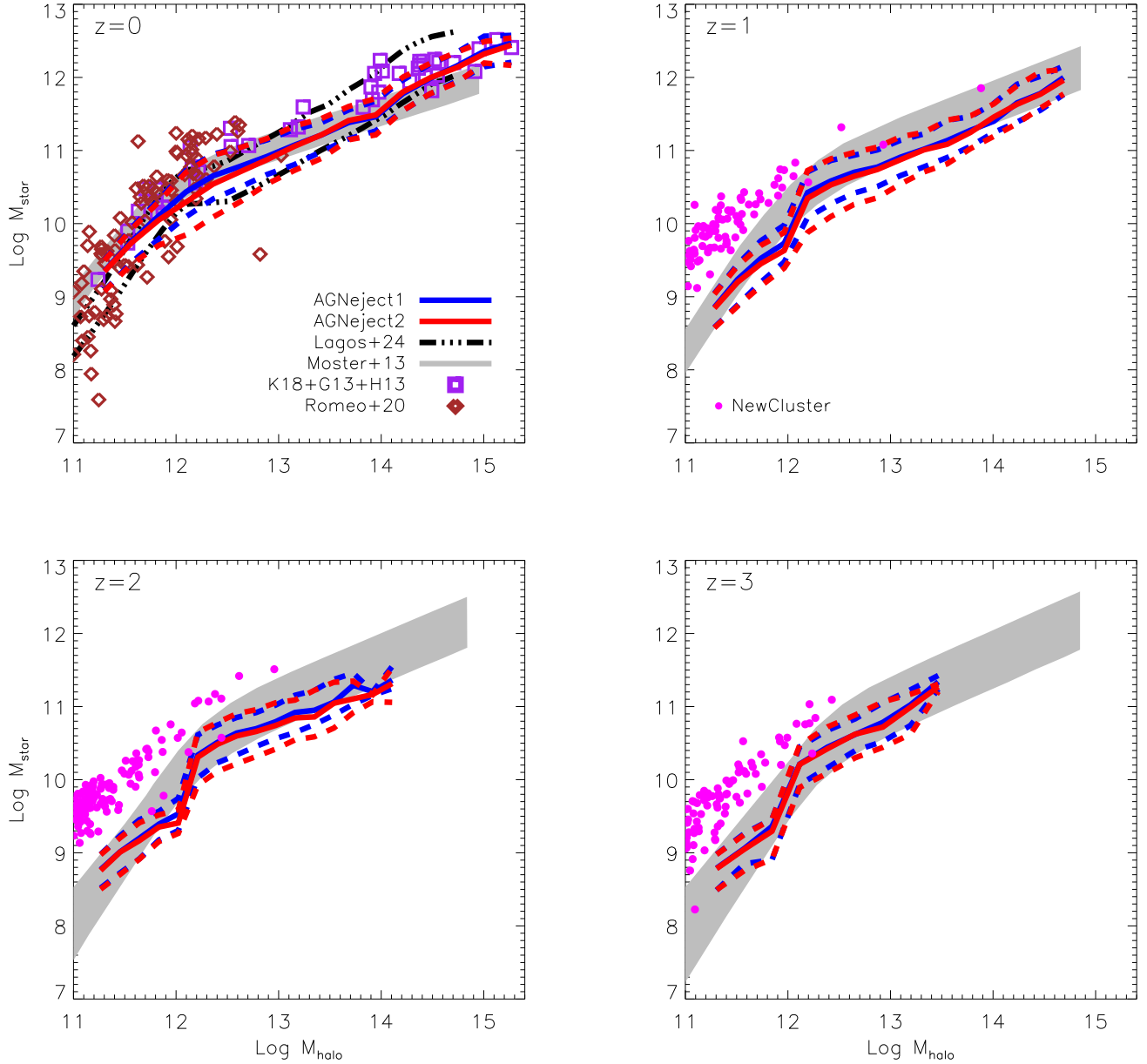


Figure 3. Stellar-to-halo mass relation for central galaxies at different redshifts (panels), as predicted by our models **AGNeject1** (blue lines) and **AGNeject2** (red lines). At $z = 0$, the predictions are compared with the SHARK2 SAM (Lagos et al. 2024), the empirical relation from Moster et al. (2013), and observational estimates from Romeo et al. (2020), Hinshaw et al. (2013), Gonzalez et al. (2013), and Kravtsov et al. (2018), as indicated in the legend. At higher redshifts ($z \geq 1$), model predictions are compared with Moster et al. (2013) and our **NewCluster** simulation. Both **AGNeject1** and **AGNeject2** show good agreement with semi-analytic, empirical, and observational constraints at $z = 0$. At higher redshifts, **NewCluster** tends to overpredict the stellar mass in low-mass halos. Accurately reproducing this relation across cosmic time is essential, as it confirms that central galaxies acquire a realistic stellar mass. This is especially crucial in low-mass halos, where the central galaxy typically accounts for the majority of stellar mass within the virial radius.

3.2. Roles of SN and AGN feedback

As mentioned several times above, SN feedback and, since the implementation of the hot gas ejection mode in C25, AGN feedback are the only mechanisms capable of expelling gas from the virialized region of halos. A key objective is to understand the level of gas expulsion

associated with each mechanism—that is, how efficient they are over time and across different halo masses.

To address this, in Figure 4 we plot the efficiency of AGN feedback as a function of halo mass for **AGNeject1** (left panel) and **AGNeject2** (right panel), at various redshifts as indicated by the color legend. We define the efficiency as

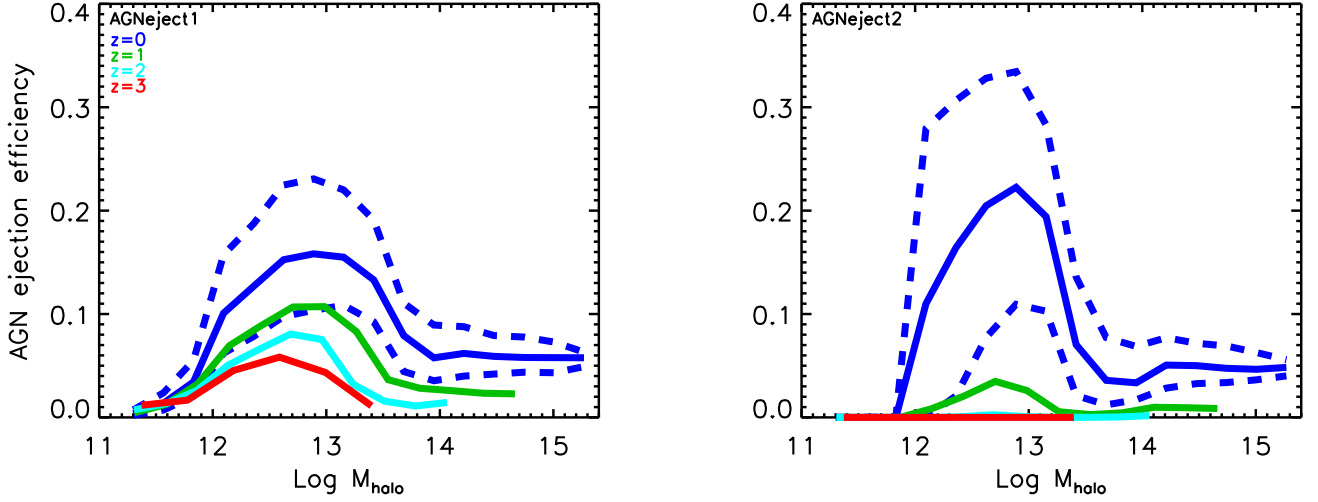


Figure 4. Efficiency of AGN feedback in ejecting gas beyond the virial radius, shown as a function of halo mass. The efficiency is defined as the total mass of gas expelled by AGN activity up to a given redshift (integrated over all progenitors in the merger tree), normalized by the halo mass at that redshift. Predictions from our two models are shown: *AGNeject1* (left panel) and *AGNeject2* (right panel), with solid lines in different colors representing different redshifts, as indicated in the legend. In *AGNeject1*, the ejection efficiency steadily increases with cosmic time, reaching a peak in the range $12.5 < \log M_{\text{halo}} < 13$, with the precise peak depending on redshift. In contrast, *AGNeject2* shows negligible efficiency across all halo masses until $z = 1$ (green line), after which the efficiency rises sharply at $\log M_{\text{halo}} > 12$, peaking around $\log M_{\text{halo}} \sim 13$ at $z = 0$. This illustrates the fundamentally different timing and strength of AGN-driven gas ejection in the two models.

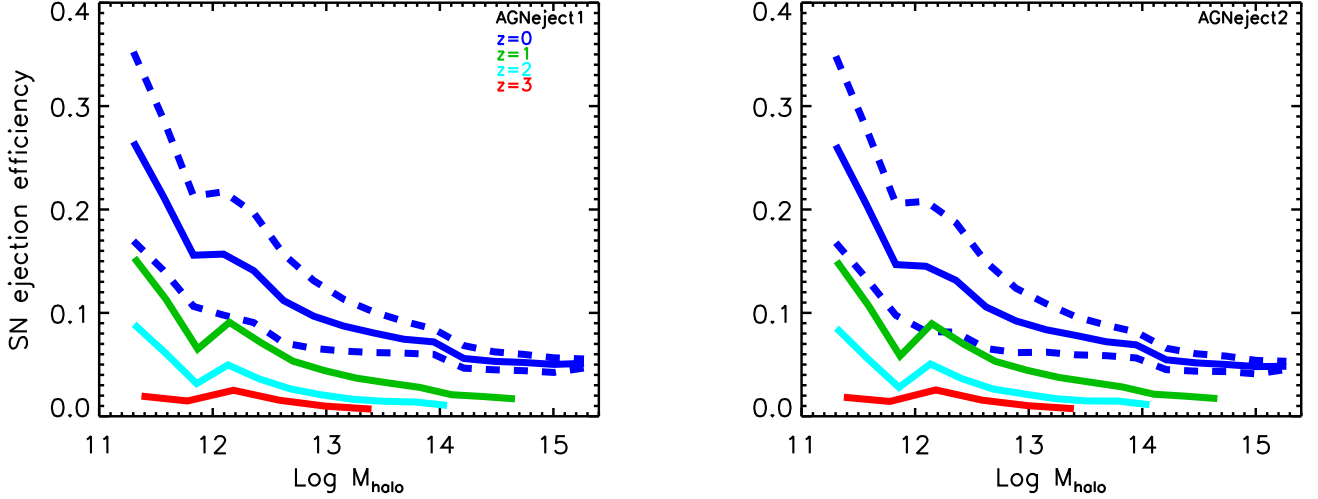


Figure 5. SN feedback efficiency as a function of halo mass for the *AGNeject1* (left) and *AGNeject2* (right) models, shown at different redshifts (color-coded lines as indicated in the legend), following the same format as Figure 4. SN feedback is most effective in low-mass halos and progressively declines with increasing halo mass. The two panels are identical, reflecting the fact that the AGN feedback implementations in these models do not influence the SN feedback.

the total amount of gas expelled by AGN feedback up to the redshift in question, accounting for all progenitors in the merger trees.

AGNeject1 exhibits a gradual increase in efficiency from high to low redshift, peaking at $z = 0$ with an efficiency of about 17% at $\log M_{\text{halo}} \sim 13$. On either side of this characteristic mass, the efficiency decreases moderately, stabilizing at approximately 5% for

$\log M_{\text{halo}} > 14$. In contrast, *AGNeject2* shows markedly different behavior. Although its efficiency profile with halo mass resembles that of *AGNeject1* at $z = 0$, the peak is higher (around 23%), and the efficiency at higher redshifts ($z > 1$) is negligible across all halo masses.

This divergence emphasizes that *AGNeject1* gradually expels hot gas over time, while *AGNeject2* remains largely inactive for about 7 Gyr and then be-

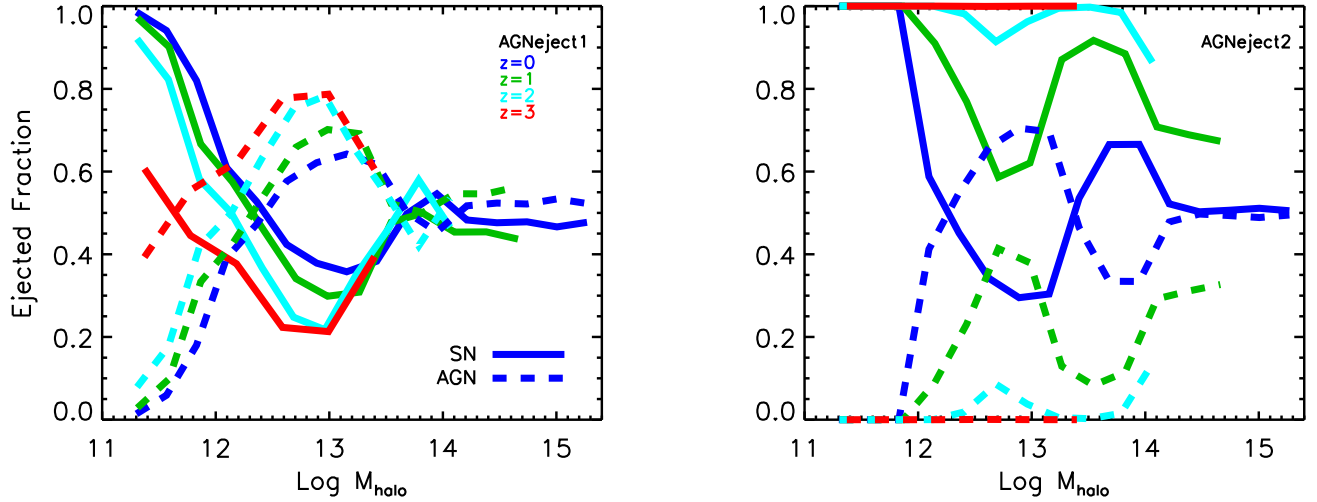


Figure 6. Fraction of gas ejected beyond the virial radius by SN (solid lines) and AGN (dashed lines) feedback, as a function of halo mass and at various redshifts (indicated by different colors), for the **AGNject1** (left panel) and **AGNject2** (right panel) models. The fractions shown represent the contribution of each feedback mode relative to the total ejected gas (i.e., SN plus AGN). The figure highlights the marked differences between the two models. In **AGNject1**, AGN feedback dominates over SN feedback in the halo mass range $11.5 < \log M_{\text{halo}} < 13.5$, depending on redshift, with the dominance centered at $\log M_{\text{halo}} \sim 13$ at $z = 0$. In contrast, **AGNject2** shows negligible AGN ejection until $z \leq 1$, after which it becomes efficient and overtakes SN feedback in the range $12.3 < \log M_{\text{halo}} < 13.2$ at $z = 0$. At the high-mass end ($\log M_{\text{halo}} > 14$), SN and AGN feedback contribute comparably in both models.

comes suddenly effective, even surpassing the performance of **AGNject1** between $0 < z < 1$. In summary, by $z = 0$, both models are most effective within the range $12 < \log M_{\text{halo}} < 14$, with an efficiency of roughly 5% on cluster scales.

In Figure 5 Roles of SN and AGN feedback figure.5, we present the counterpart of Figure 4 Roles of SN and AGN feedback figure.4 for SN feedback. At first glance, it is evident that both models behave identically in this case, indicating that AGN feedback does not influence the behavior of SN feedback. The efficiency of SN feedback decreases with halo mass and increases with redshift. The smallest halos in our sample experience the strongest SN feedback, with efficiencies reaching up to 30%, while even on cluster scales the efficiency remains non-negligible at around 5%. It is worth emphasizing that on cluster scales, the efficiencies of SN and AGN feedback are comparable—an important and non-trivial result.

To directly compare SN and AGN feedback within the same framework, in Figure 6 Roles of SN and AGN feedback figure.6 we plot their respective contributions to the total gas expelled as a function of halo mass and redshift. SN feedback is represented by solid lines, and AGN feedback by dashed lines, with different colors indicating redshift. The left and right panels correspond to the **AGNject1** and **AGNject2** models, respectively. The two models display clearly distinct behaviors: **AGNject1** shows a weak dependence on red-

shift, whereas **AGNject2** exhibits a strong redshift dependence, as expected from its delayed onset of AGN activity.

Notably, in both models, SN feedback dominates the total gas expulsion except within the characteristic mass ranges where AGN feedback becomes particularly efficient. Specifically, AGN feedback dominates in halos with $12.5 < \log M_{\text{halo}} < 13.5$ for **AGNject1**, and $12.2 < \log M_{\text{halo}} < 13.3$ for **AGNject2**, both at $z = 0$. Thus, SN feedback is the primary driver of gas ejection in low-mass and Milky Way-like halos, while AGN feedback takes over in the subsequent mass decade, with both mechanisms contributing roughly equally on large group and cluster scales.

Our findings are qualitatively consistent with those of Ayromlou et al. (2023) (but see also the analysis in Wright et al. 2024), who analyzed three sets of cosmological hydrodynamic simulations—EAGLE (Schaye et al. 2015), IllustrisTNG (Pillepich et al. 2018), and SIMBA (Davé et al. 2019). These authors showed that feedback processes play a crucial role in redistributing gas within and beyond halo boundaries, reducing the baryon fraction inside halos and transferring hot gas outside the virial radius.

A particularly interesting result from their study is the concept of the closure radius—the radius at which the enclosed baryon fraction equals the universal value. They found that the closure radius decreases with increasing halo mass. For instance, in low-mass halos with

$\log M_{\text{halo}} = 11$, this radius can be as large as 5–10 times the virial radius, depending on the simulation. In contrast, for massive groups and clusters, the closure radius lies within the virial radius itself.

While our models predict baryon fractions of about 75% in massive halos—somewhat lower than the closure point identified in the simulations—there is strong agreement regarding the mass dependence of feedback efficiency: both SN and AGN feedback are found to be critical in similar halo mass ranges.

To conclude this section, we now turn to a detailed comparison between the baryon fractions predicted by our models and those reported by [Ayromlou et al. \(2023\)](#) in their analysis.

3.3. *FEGA25 vs Simulations*

We end our analysis with a full comparison between our models and predictions from hydrodynamic simulations. [Ayromlou et al. \(2023\)](#) convincingly demonstrated that the EAGLE, IllustrisTNG, and SIMBA simulations all predict different baryon fractions as a function of halo mass, emphasizing that the baryonic content of halos is highly sensitive to the specific physical processes implemented in each model.

In Figure 7 *FEGA25 vs Simulations* figure.7, we show the baryon fraction—normalized to the universal value—as a function of halo mass at $z = 0$, as predicted by our models: **AGNeject1** (left panel) and **AGNeject2** (right panel). For comparison, we also overplot the predictions from the above-mentioned simulations, with colors indicated in the legend. It is evident that both the simulations and our models predict significantly different baryon fractions and trends. Nonetheless, some common features can be identified across the simulations. First, they all converge on cluster scales ($\log M_{\text{halo}} > 14$), where the baryon fraction approaches the universal value. Second, while EAGLE exhibits a monotonic increase in baryon fraction from low to high halo masses, both IllustrisTNG and SIMBA show a pronounced dip—that we named cavity—in the intermediate-mass range, a feature also present in our model **AGNeject2**. However, the location, width, and depth of this cavity vary substantially among the simulations.

From this comparison, we can conclude that **AGNeject1** aligns more closely with EAGLE in terms of the general trend, particularly the absence of a cavity. Conversely, **AGNeject2**, especially for $\log M_{\text{halo}} < 13.7$, resembles the behavior seen in both IllustrisTNG and SIMBA. Given the observational comparisons shown in Figures 1 *The Baryonic Content in DM Halos* figure.1 and 2 *The Baryonic Content in DM Halos* figure.2, and especially considering the large scatter in the data, we con-

clude that it is currently not possible to rule out any of the models or the physical assumptions implemented in them. To determine whether the cavity is a genuine feature, more observational data are needed for halos with $\log M_{\text{halo}} < 12$, including accurate measurements of both baryon and hot gas fractions, and with reduced observational scatter.

A similar comparison between observations and simulations was recently presented by [Popesso et al. \(2024\)](#). Using the public Early Data Release (EDR) eROSITA event file of the eFEDS field ([Brunner et al. 2022](#)), they compared the hot gas fraction within R_{500} with predictions from a wide array of simulations, including: BAHAMAS ([Salcido et al. 2023](#)), FLAMINGO ([Schaye et al. 2023](#)), IllustrisTNG, MAGNETICUM, SIMBA, and MillenniumTNG ([Pakmor et al. 2023](#)). Their findings indicate that IllustrisTNG and MillenniumTNG—both of which share similar physical models—tend to overpredict the observed hot gas fractions at nearly all halo masses. On the other hand, FLAMINGO and BAHAMAS, which implement similar AGN feedback schemes, are more consistent with observations. Among all the simulations, only MAGNETICUM reproduces the observed relation remarkably well, while SIMBA does so within the 1σ scatter, albeit with somewhat lower agreement. Notably, MAGNETICUM—the most observationally consistent model—does not exhibit a cavity as seen in some other simulations and in our model **AGNeject2**, but instead follows a power-law trend, similar to that observed.

To conclude, the comparison of our models with both simulations and observations shows a broad range of behaviors. Some simulations—as well as our model **AGNeject2**—predict a cavity in the baryon and hot gas fractions, while others—including our model **AGNeject1**—do not. Current observations tend to support a power-law behavior in both relations. However, as emphasized above, probing scales below $\log M_{\text{halo}} \sim 12$ is essential before making definitive conclusions about the validity of the physical prescriptions used in simulations and semianalytic models.

In light of these findings, we present our final conclusions in the next section.

4. CONCLUSIONS

In our state-of-the-art semi-analytic model, **FEGA25**, we have implemented an additional mechanism—alongside SN feedback—for ejecting hot gas beyond the virial radius of halos. This mechanism is directly associated with AGN feedback and is realized in two different forms: the **AGNeject1** model, identical to the one introduced in [Contini et al. \(2025\)](#), and the

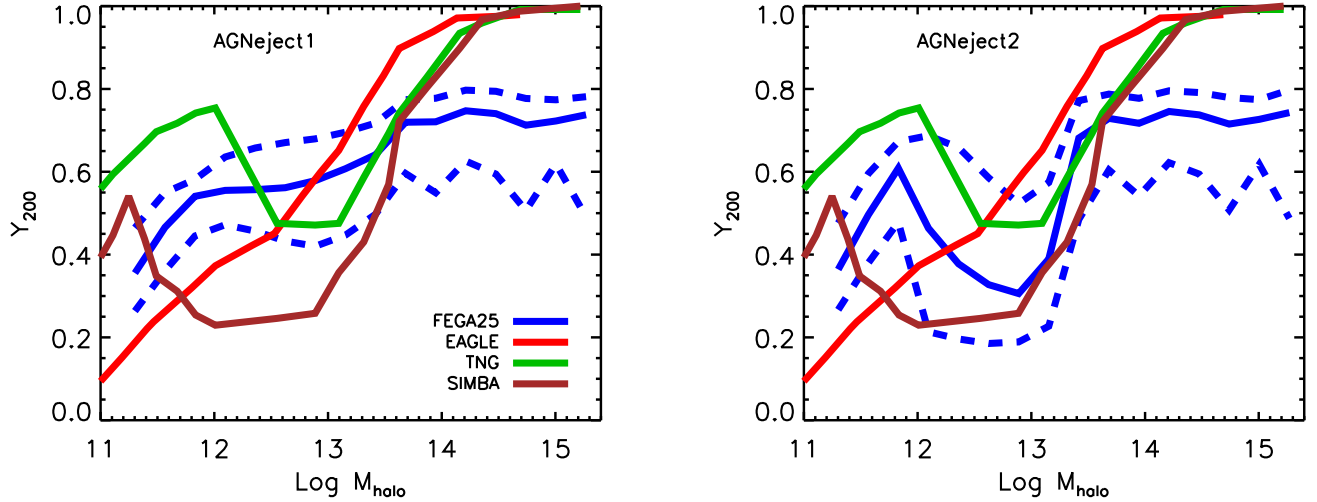


Figure 7. Baryon fraction normalized to the universal value as a function of halo mass at $z = 0$, as predicted by **AGNeject1** (left panel) and **AGNeject2** (right panel). Model predictions are compared with three hydrodynamical simulations: EAGLE (Schaye et al. 2015, red), IllustrisTNG (Pillepich et al. 2018, green), and SIMBA (Davé et al. 2019, brown). While neither of our models reproduces the simulation results across the entire halo mass range, **AGNeject2** exhibits a qualitative similarity with IllustrisTNG and SIMBA: all three show a distinct “cavity” in the baryon fraction, albeit with varying depth and located at different halo masses. A notable feature of the simulations is the rise of the baryon fraction toward the universal value on cluster scales, whereas our models continue to predict a significant baryon deficit (about 25%) even at the high-mass end, indicating that a substantial amount of baryons remains outside the virialized region.

AGNeject2 model, which differs in strength and becomes primarily active at $z < 1$.

Our models predict baryon and hot gas fractions as a function of halo mass in broad agreement with current observational constraints. Notably, while **AGNeject1** yields a monotonic increase in both fractions with halo mass, **AGNeject2** predicts a distinct cavity at halo masses below $\log M_{\text{halo}} \sim 13$, a feature commonly seen in several hydrodynamic simulations. Furthermore, **AGNeject2** exhibits a redshift dependence in the mass range where the cavity appears, while **AGNeject1** shows minimal evolution. The primary difference between the two models lies in the time-dependent strength of AGN feedback; however, both are capable of efficiently ejecting hot gas from halos.

Both models successfully reproduce the stellar-to-halo mass relation up to $z = 3$, and match observational data at $z = 0$, which is a significant achievement given the broad dynamic range in both halo mass and redshift. This success is particularly relevant in the context of the hot gas content in galaxy groups, where the cold gas fraction becomes negligible. The implication is that any viable numerical method must include a mechanism that can remove hot gas without significantly altering the stellar and cold gas components—consistent with recent observational findings.

Our results also highlight the relative importance of SN and AGN feedback across different halo mass scales. In line with recent hydrodynamic simulation results at

$z = 0$ —which we extend to higher redshifts—we find that SN feedback dominates for $\log M_{\text{halo}} \lesssim 12.5$, while AGN feedback becomes increasingly significant at higher halo masses. On group and cluster scales, both feedback mechanisms contribute comparably. However, at higher redshifts, the models diverge: **AGNeject1** maintains a nearly constant division between SN and AGN feedback, whereas **AGNeject2** exhibits significant evolution, with SN feedback remaining dominant down to $z = 1$, at all scales.

When compared to both simulations and observations, the two models show differing levels of agreement depending on the specific regime. **AGNeject1** is more consistent with observational data, as it predicts a smooth, monotonic increase in baryon and hot gas fractions with halo mass. In contrast, **AGNeject2** reproduces the cavity seen in several simulations. Nonetheless, we do not discard either model. The lack of observational data at small halo masses—particularly below $\log M_{\text{halo}} \sim 12.5$ —where **AGNeject2** and several simulations predict a re-rise in the gas fractions, coupled with the significant observational scatter at all mass scales, makes it premature to rule out any model. In order to assess the physical plausibility of the cavity, and thus constrain the most realistic feedback mechanism, more observational data are needed below $\log M_{\text{halo}} \sim 12$ – 12.5 , with significantly reduced scatter (ideally at least a third to half of the current levels).

Despite the differing predictions of the two models, one robust conclusion emerges: as also supported by observational evidence, SN feedback alone is insufficient to account for the ejection of hot gas. Several simulation-based studies, along with our current semi-analytic implementation, demonstrate that AGN feedback in the form of hot gas ejection is a viable and necessary mechanism. Therefore, it must be included—and ideally refined—in any numerical framework aiming to accurately model galaxy formation and the baryon cycle in halos.

ACKNOWLEDGEMENTS

E.C. and S.K.Y. acknowledge support from the Korean National Research Foundation (RS-2025-00514475). E.C. and S.J. acknowledge support from

the Korean National Research Foundation (RS-2023-00241934). All the authors are supported by the Korean National Research Foundation (RS-2022-NR070872). J.R. was supported by the KASI-Yonsei Postdoctoral Fellowship and by the Korea Astronomy and Space Science Institute under the R&D program (Project No. 2023-1-830-00), supervised by the Ministry of Science and ICT. This work was also partially supported by the Institut de Physique des deux infinis of Sorbonne Université and by the ANR grant ANR-19-CE31-0017 of the French Agence Nationale de la Recherche.

DATA AVAILABILITY

Codes and galaxy catalogs used in this study can be obtained by contacting the corresponding author.

REFERENCES

- Akino, D., Eckert, D., Okabe, N., et al. 2022, *PASJ*, 74, 175, doi: [10.1093/pasj/psab115](https://doi.org/10.1093/pasj/psab115)
- Angelinelli, M., Ettori, S., Dolag, K., Vazza, F., & Ragagnin, A. 2023, *A&A*, 675, A188, doi: [10.1051/0004-6361/202245782](https://doi.org/10.1051/0004-6361/202245782)
- Arnaud, M., Pointecouteau, E., & Pratt, G. W. 2007, *A&A*, 474, L37, doi: [10.1051/0004-6361:20078541](https://doi.org/10.1051/0004-6361:20078541)
- Ayromlou, M., Nelson, D., & Pillepich, A. 2023, *MNRAS*, 524, 5391, doi: [10.1093/mnras/stad2046](https://doi.org/10.1093/mnras/stad2046)
- Baldry, I. K., Glazebrook, K., & Driver, S. P. 2008, *MNRAS*, 388, 945, doi: [10.1111/j.1365-2966.2008.13348.x](https://doi.org/10.1111/j.1365-2966.2008.13348.x)
- Baldry, I. K., Driver, S. P., Loveday, J., et al. 2012, *MNRAS*, 421, 621, doi: [10.1111/j.1365-2966.2012.20340.x](https://doi.org/10.1111/j.1365-2966.2012.20340.x)
- Behroozi, P., Wechsler, R. H., Hearin, A. P., & Conroy, C. 2019, *MNRAS*, 488, 3143, doi: [10.1093/mnras/stz1182](https://doi.org/10.1093/mnras/stz1182)
- Bernardi, M., Sheth, R. K., Dominguez-Sanchez, H., et al. 2018, *MNRAS*, 477, 2560, doi: [10.1093/mnras/sty781](https://doi.org/10.1093/mnras/sty781)
- Brunner, H., Liu, T., Lamer, G., et al. 2022, *A&A*, 661, A1, doi: [10.1051/0004-6361/202141266](https://doi.org/10.1051/0004-6361/202141266)
- Chabrier, G. 2003, *PASP*, 115, 763, doi: [10.1086/376392](https://doi.org/10.1086/376392)
- Chiu, I., Mohr, J., McDonald, M., et al. 2016, *MNRAS*, 455, 258, doi: [10.1093/mnras/stv2303](https://doi.org/10.1093/mnras/stv2303)
- Contini, E., Gu, Q., Ge, X., et al. 2020, *ApJ*, 889, 156, doi: [10.3847/1538-4357/ab6730](https://doi.org/10.3847/1538-4357/ab6730)
- Contini, E., Gu, Q., Kang, X., Rhee, J., & Yi, S. K. 2019, *ApJ*, 882, 167, doi: [10.3847/1538-4357/ab3b03](https://doi.org/10.3847/1538-4357/ab3b03)
- Contini, E., Jeon, S., Rhee, J., Han, S., & Yi, S. K. 2023, *ApJ*, 958, 72, doi: [10.3847/1538-4357/acfd25](https://doi.org/10.3847/1538-4357/acfd25)
- Contini, E., Kang, X., Romeo, A. D., & Xia, Q. 2017, *ApJ*, 837, 27, doi: [10.3847/1538-4357/aa5d16](https://doi.org/10.3847/1538-4357/aa5d16)
- Contini, E., Yi, S. K., Jeon, S., & Rhee, J. 2024, *ApJS*, 274, 41, doi: [10.3847/1538-4365/ad70ac](https://doi.org/10.3847/1538-4365/ad70ac)
- Contini, E., Yi, S. K., Rhee, J., & Jeon, S. 2025, arXiv e-prints, arXiv:2502.19503, doi: [10.48550/arXiv.2502.19503](https://doi.org/10.48550/arXiv.2502.19503)
- Cresci, G., Mainieri, V., Brusa, M., et al. 2015, *ApJ*, 799, 82, doi: [10.1088/0004-637X/799/1/82](https://doi.org/10.1088/0004-637X/799/1/82)
- Croton, D. J., Springel, V., White, S. D. M., et al. 2006, *MNRAS*, 365, 11, doi: [10.1111/j.1365-2966.2005.09675.x](https://doi.org/10.1111/j.1365-2966.2005.09675.x)
- Davé, R., Anglés-Alcázar, D., Narayanan, D., et al. 2019, *MNRAS*, 486, 2827, doi: [10.1093/mnras/stz937](https://doi.org/10.1093/mnras/stz937)
- Dev, A., Driver, S. P., Meyer, M., et al. 2024, *MNRAS*, 535, 2357, doi: [10.1093/mnras/stae2485](https://doi.org/10.1093/mnras/stae2485)
- Dolag, K., Komatsu, E., & Sunyaev, R. 2016, *MNRAS*, 463, 1797, doi: [10.1093/mnras/stw2035](https://doi.org/10.1093/mnras/stw2035)
- Dubois, Y., Devriendt, J., Slyz, A., & Teyssier, R. 2012, *MNRAS*, 420, 2662, doi: [10.1111/j.1365-2966.2011.20236.x](https://doi.org/10.1111/j.1365-2966.2011.20236.x)
- Eckert, D., Gaspari, M., Gastaldello, F., Le Brun, A. M. C., & O'Sullivan, E. 2021, *Universe*, 7, 142, doi: [10.3390/universe7050142](https://doi.org/10.3390/universe7050142)
- Eckert, D., Ettori, S., Coupon, J., et al. 2016, *A&A*, 592, A12, doi: [10.1051/0004-6361/201527293](https://doi.org/10.1051/0004-6361/201527293)
- Eckert, D., Ghirardini, V., Ettori, S., et al. 2019, *A&A*, 621, A40, doi: [10.1051/0004-6361/201833324](https://doi.org/10.1051/0004-6361/201833324)
- Gaibler, V., Khochfar, S., Krause, M., & Silk, J. 2012, *MNRAS*, 425, 438, doi: [10.1111/j.1365-2966.2012.21479.x](https://doi.org/10.1111/j.1365-2966.2012.21479.x)
- Gonzalez, A. H., Sivanandam, S., Zabludoff, A. I., & Zaritsky, D. 2013, *ApJ*, 778, 14, doi: [10.1088/0004-637X/778/1/14](https://doi.org/10.1088/0004-637X/778/1/14)
- Guo, Q., White, S., Angulo, R. E., et al. 2013, *MNRAS*, 428, 1351, doi: [10.1093/mnras/sts115](https://doi.org/10.1093/mnras/sts115)
- Guo, Q., White, S., Li, C., & Boylan-Kolchin, M. 2010, *MNRAS*, 404, 1111, doi: [10.1111/j.1365-2966.2010.16341.x](https://doi.org/10.1111/j.1365-2966.2010.16341.x)

- Guo, Q., White, S., Boylan-Kolchin, M., et al. 2011, MNRAS, 413, 101, doi: [10.1111/j.1365-2966.2010.18114.x](https://doi.org/10.1111/j.1365-2966.2010.18114.x)
- Hadzhiyska, B., Ferraro, S., Ried Guachalla, B., et al. 2024, arXiv e-prints, arXiv:2407.07152, doi: [10.48550/arXiv.2407.07152](https://doi.org/10.48550/arXiv.2407.07152)
- Han, S., Dubois, Y., Lee, J., et al. 2025a, ApJ, 978, 96, doi: [10.3847/1538-4357/ad98f4](https://doi.org/10.3847/1538-4357/ad98f4)
- Han, S., Yi, S. K., Dubois, Y., et al. 2025b, arXiv e-prints, arXiv:2507.06301. <https://arxiv.org/abs/2507.06301>
- Henriques, B. M. B., White, S. D. M., Thomas, P. A., et al. 2015, MNRAS, 451, 2663, doi: [10.1093/mnras/stv705](https://doi.org/10.1093/mnras/stv705)
- . 2013, MNRAS, 431, 3373, doi: [10.1093/mnras/stt415](https://doi.org/10.1093/mnras/stt415)
- Henriques, B. M. B., Yates, R. M., Fu, J., et al. 2020, MNRAS, 491, 5795, doi: [10.1093/mnras/stz3233](https://doi.org/10.1093/mnras/stz3233)
- Hinshaw, G., Larson, D., Komatsu, E., et al. 2013, ApJS, 208, 19, doi: [10.1088/0067-0049/208/2/19](https://doi.org/10.1088/0067-0049/208/2/19)
- Hirschmann, M., De Lucia, G., & Fontanot, F. 2016, MNRAS, 461, 1760, doi: [10.1093/mnras/stw1318](https://doi.org/10.1093/mnras/stw1318)
- Ilbert, O., Salvato, M., Le Floch, E., et al. 2010, ApJ, 709, 644, doi: [10.1088/0004-637X/709/2/644](https://doi.org/10.1088/0004-637X/709/2/644)
- Ilbert, O., McCracken, H. J., Le Fèvre, O., et al. 2013, A&A, 556, A55, doi: [10.1051/0004-6361/201321100](https://doi.org/10.1051/0004-6361/201321100)
- Iwamoto, K., Brachwitz, F., Nomoto, K., et al. 1999, ApJS, 125, 439, doi: [10.1086/313278](https://doi.org/10.1086/313278)
- Joseph, P., Sreekumar, P., Stalin, C. S., et al. 2022, MNRAS, 516, 2300, doi: [10.1093/mnras/stac2388](https://doi.org/10.1093/mnras/stac2388)
- Kimm, T., & Cen, R. 2014, ApJ, 788, 121, doi: [10.1088/0004-637X/788/2/121](https://doi.org/10.1088/0004-637X/788/2/121)
- Kobayashi, C., Umeda, H., Nomoto, K., Tominaga, N., & Ohkubo, T. 2006, ApJ, 653, 1145, doi: [10.1086/508914](https://doi.org/10.1086/508914)
- Komatsu, E., Smith, K. M., Dunkley, J., et al. 2011, ApJS, 192, 18, doi: [10.1088/0067-0049/192/2/18](https://doi.org/10.1088/0067-0049/192/2/18)
- Kravtsov, A. V., Vikhlinin, A. A., & Meshcheryakov, A. V. 2018, Astronomy Letters, 44, 8, doi: [10.1134/S1063773717120015](https://doi.org/10.1134/S1063773717120015)
- Lagos, C. d. P., Bravo, M., Tobar, R., et al. 2024, MNRAS, 531, 3551, doi: [10.1093/mnras/stae1024](https://doi.org/10.1093/mnras/stae1024)
- Leitherer, C., Schaerer, D., Goldader, J. D., et al. 1999, ApJS, 123, 3, doi: [10.1086/313233](https://doi.org/10.1086/313233)
- Li, C., & White, S. D. M. 2009, MNRAS, 398, 2177, doi: [10.1111/j.1365-2966.2009.15268.x](https://doi.org/10.1111/j.1365-2966.2009.15268.x)
- Lovisari, L., Reiprich, T. H., & Schellenberger, G. 2015, A&A, 573, A118, doi: [10.1051/0004-6361/201423954](https://doi.org/10.1051/0004-6361/201423954)
- Madau, P., & Dickinson, M. 2014, ARA&A, 52, 415, doi: [10.1146/annurev-astro-081811-125615](https://doi.org/10.1146/annurev-astro-081811-125615)
- Mahdavi, A., Hoekstra, H., Babul, A., et al. 2013, ApJ, 767, 116, doi: [10.1088/0004-637X/767/2/116](https://doi.org/10.1088/0004-637X/767/2/116)
- Mahoro, A., Pović, M., & Nkundabakura, P. 2017, MNRAS, 471, 3226, doi: [10.1093/mnras/stx1762](https://doi.org/10.1093/mnras/stx1762)
- Marchesini, D., van Dokkum, P. G., Förster Schreiber, N. M., et al. 2009, ApJ, 701, 1765, doi: [10.1088/0004-637X/701/2/1765](https://doi.org/10.1088/0004-637X/701/2/1765)
- Marchesini, D., Whitaker, K. E., Brammer, G., et al. 2010, ApJ, 725, 1277, doi: [10.1088/0004-637X/725/1/1277](https://doi.org/10.1088/0004-637X/725/1/1277)
- Moster, B. P., Naab, T., & White, S. D. M. 2013, MNRAS, 428, 3121, doi: [10.1093/mnras/sts261](https://doi.org/10.1093/mnras/sts261)
- Mukherjee, D., Bicknell, G. V., Wagner, A. Y., Sutherland, R. S., & Silk, J. 2018, MNRAS, 479, 5544, doi: [10.1093/mnras/sty1776](https://doi.org/10.1093/mnras/sty1776)
- Mulroy, S. L., Farahi, A., Evrard, A. E., et al. 2019, MNRAS, 484, 60, doi: [10.1093/mnras/sty3484](https://doi.org/10.1093/mnras/sty3484)
- Muzzin, A., Marchesini, D., Stefanon, M., et al. 2013, ApJ, 777, 18, doi: [10.1088/0004-637X/777/1/18](https://doi.org/10.1088/0004-637X/777/1/18)
- Naab, T., & Ostriker, J. P. 2017, ARA&A, 55, 59, doi: [10.1146/annurev-astro-081913-040019](https://doi.org/10.1146/annurev-astro-081913-040019)
- Nelson, D., Springel, V., Pillepich, A., et al. 2019, Computational Astrophysics and Cosmology, 6, 2, doi: [10.1186/s40668-019-0028-x](https://doi.org/10.1186/s40668-019-0028-x)
- Pakmor, R., Springel, V., Coles, J. P., et al. 2023, MNRAS, 524, 2539, doi: [10.1093/mnras/stac3620](https://doi.org/10.1093/mnras/stac3620)
- Pearson, R. J., Ponman, T. J., Norberg, P., et al. 2017, MNRAS, 469, 3489, doi: [10.1093/mnras/stx1081](https://doi.org/10.1093/mnras/stx1081)
- Pillepich, A., Nelson, D., Hernquist, L., et al. 2018, MNRAS, 475, 648, doi: [10.1093/mnras/stx3112](https://doi.org/10.1093/mnras/stx3112)
- Planck Collaboration, Aghanim, N., Akrami, Y., et al. 2020, A&A, 641, A6, doi: [10.1051/0004-6361/201833910](https://doi.org/10.1051/0004-6361/201833910)
- Popesso, P., Biviano, A., Marini, I., et al. 2024, arXiv e-prints, arXiv:2411.16555, doi: [10.48550/arXiv.2411.16555](https://doi.org/10.48550/arXiv.2411.16555)
- Pratt, G. W., Croston, J. H., Arnaud, M., & Böhringer, H. 2009, A&A, 498, 361, doi: [10.1051/0004-6361/200810994](https://doi.org/10.1051/0004-6361/200810994)
- Ragagnin, A., Andreon, S., & Puddu, E. 2022, A&A, 666, A22, doi: [10.1051/0004-6361/202244397](https://doi.org/10.1051/0004-6361/202244397)
- Rasmussen, J., & Ponman, T. J. 2009, MNRAS, 399, 239, doi: [10.1111/j.1365-2966.2009.15244.x](https://doi.org/10.1111/j.1365-2966.2009.15244.x)
- Romeo, A. B., Agertz, O., & Renaud, F. 2020, MNRAS, 499, 5656, doi: [10.1093/mnras/staa3245](https://doi.org/10.1093/mnras/staa3245)
- Salcido, J., McCarthy, I. G., Kwan, J., Upadhye, A., & Font, A. S. 2023, MNRAS, 523, 2247, doi: [10.1093/mnras/stad1474](https://doi.org/10.1093/mnras/stad1474)
- Sánchez, S. F., Kennicutt, R. C., & Gil de Paz, e. a. 2012, A&A, 538, A8, doi: [10.1051/0004-6361/201117353](https://doi.org/10.1051/0004-6361/201117353)
- Schaye, J., Crain, R. A., Bower, R. G., et al. 2015, MNRAS, 446, 521, doi: [10.1093/mnras/stu2058](https://doi.org/10.1093/mnras/stu2058)
- Schaye, J., Kugel, R., Schaller, M., et al. 2023, MNRAS, 526, 4978, doi: [10.1093/mnras/stad2419](https://doi.org/10.1093/mnras/stad2419)
- Shi, Y., Helou, G., Yan, L., et al. 2011, ApJ, 733, 87, doi: [10.1088/0004-637X/733/2/87](https://doi.org/10.1088/0004-637X/733/2/87)

- Silk, J. 2013, *ApJ*, 772, 112,
doi: [10.1088/0004-637X/772/2/112](https://doi.org/10.1088/0004-637X/772/2/112)
- Somerville, R. S., & Davé, R. 2015, *ARA&A*, 53, 51,
doi: [10.1146/annurev-astro-082812-140951](https://doi.org/10.1146/annurev-astro-082812-140951)
- Springel, V., Pakmor, R., Zier, O., & Reinecke, M. 2021,
MNRAS, 506, 2871, doi: [10.1093/mnras/stab1855](https://doi.org/10.1093/mnras/stab1855)
- Springel, V., White, S. D. M., Jenkins, A., et al. 2005,
Nature, 435, 629, doi: [10.1038/nature03597](https://doi.org/10.1038/nature03597)
- Sun, M., Voit, G. M., Donahue, M., et al. 2009, *ApJ*, 693,
1142, doi: [10.1088/0004-637X/693/2/1142](https://doi.org/10.1088/0004-637X/693/2/1142)
- Teyssier, R. 2002, *A&A*, 385, 337,
doi: [10.1051/0004-6361:20011817](https://doi.org/10.1051/0004-6361:20011817)
- Tomczak, A. R., Quadri, R. F., Tran, K.-V. H., et al. 2014,
ApJ, 783, 85, doi: [10.1088/0004-637X/783/2/85](https://doi.org/10.1088/0004-637X/783/2/85)
- Vikhlinin, A., Kravtsov, A., Forman, W., et al. 2006, *ApJ*,
640, 691, doi: [10.1086/500288](https://doi.org/10.1086/500288)
- Vogelsberger, M., Marinacci, F., Torrey, P., & Puchwein, E.
2020, *Nature Reviews Physics*, 2, 42,
doi: [10.1038/s42254-019-0127-2](https://doi.org/10.1038/s42254-019-0127-2)
- White, S. D. M., & Rees, M. J. 1978, *MNRAS*, 183, 341,
doi: [10.1093/mnras/183.3.341](https://doi.org/10.1093/mnras/183.3.341)
- Wright, R. J., Somerville, R. S., Lagos, C. d. P., et al. 2024,
MNRAS, 532, 3417, doi: [10.1093/mnras/stae1688](https://doi.org/10.1093/mnras/stae1688)